Supercritical CO_2 uptake by nonswelling phyllosilicates

Jiamin Wan[a,1], Tetsu K. Tokunaga[a], Paul D. Ashby[b], Yongman Kim[a], Marco Voltolini[a], Benjamin Gilbert[a], and Donald J. DePaolo[a,1]

[a]Energy Geosciences Division, Earth and Environment Sciences Area, Lawrence Berkeley National Laboratory, Berkeley, CA 94720; and [b]The Molecular Foundry, Material Sciences Division, Lawrence Berkeley National Laboratory, Berkeley, CA 94720

Contributed by Donald J. DePaolo, September 2, 2017 (sent for review June 23, 2017; reviewed by Andreas Busch and Andrey Kalinichev)

Interactions between supercritical (sc) CO_2 and minerals are important when CO_2 is injected into geologic formations for storage and as working fluids for enhanced oil recovery, hydraulic fracturing, and geothermal energy extraction. It has previously been shown that at the elevated pressures and temperatures of the deep subsurface, $scCO_2$ alters smectites (typical swelling phyllosilicates). However, less is known about the effects of $scCO_2$ on nonswelling phyllosilicates (illite and muscovite), despite the fact that the latter are the dominant clay minerals in deep subsurface shales and mudstones. Our studies conducted by using single crystals, combining reaction (incubation with $scCO_2$), visualization [atomic force microscopy (AFM)], and quantifications (AFM, X-ray photoelectron spectroscopy, X-ray diffraction, and off-gassing measurements) revealed unexpectedly high CO_2 uptake that far exceeded its macroscopic surface area. Results from different methods collectively suggest that CO_2 partially entered the muscovite interlayers, although the pathways remain to be determined. We hypothesize that preferential dissolution at weaker surface defects and frayed edges allows CO_2 to enter the interlayers under elevated pressure and temperature, rather than by diffusing solely from edges deeply into interlayers. This unexpected uptake of CO_2, can increase CO_2 storage capacity by up to ∼30% relative to the capacity associated with residual trapping in a 0.2-porosity sandstone reservoir containing up to 18 mass % of illite/muscovite. This excess CO_2 uptake constitutes a previously unrecognized potential trapping mechanism.

carbon sequestration | CO_2 uptake | nonswelling phyllosilicates | muscovite | illite

CO_2 is increasingly used in many deep subsurface engineering processes, such as enhanced oil recovery, geological carbon storage in saline formations, depleted gas and oil fields (1, 2), waterless hydraulic fracturing, and enhanced geothermal systems (3, 4). Tight rocks (shales and mudstones) function as caprocks in geological CO_2 sequestration and as host rocks in unconventional gas and oil extractions. Reactions with supercritical CO_2 ($scCO_2$) under elevated pressure and temperature conditions of the deep subsurface can significantly change physical and chemical properties of rocks and minerals. CO_2 uptake can lead to rock volume expansion, increased rock stress, and geomechanical deformation (5–7). Wettability alteration resulting from $scCO_2$ reactions has been reported by a number of researchers (8–10), although the measurements can contain large uncertainties (11). Dewetting and changes in capillary forces controlling saturation have been reported to result from long-term exposure to $scCO_2$ (12–16), and strong CO_2 adsorption can increase CO_2 storage capacity and CO_2 preferential adsorption enhance petroleum gas release (17, 18).

Wilson et al. (19) reviewed the mineralogy of the major unconventional hydrocarbon shale reservoirs in the United States and reported that the clay mineralogy of practically all of the shale reservoirs older than the Upper Cretaceous is dominated by illitic clay, as discrete illite and/or mixed-layer illite/smectite. There is no occurrence of smectite as a discrete phase in the shale formations older than the Upper Cretaceous, although it is not clear whether all of the illite is derived through illitization of a smectite precursor (19). The name "illite," given by Grim, Bray, and Bradley in 1937 (20), is a general term for the mica-type mineral with 10-Å spacing that does not expand on treatment with glycol. Although illite belongs to the mica group, compared with the well-crystallized micas, illite has a lower degree of order, smaller particle size, lower potassium content, and variable cation population in its tetrahedral and octahedral structure (20). Smectite is a swelling or expandable clay with the interlayer spacing dependent on hydration state and counterion occupancy. Many recent studies reported that smectites have strong CO_2 adsorption capacity and that CO_2 can intercalate into smectite interlayers (21–29). Espinoza and Santamarina (30) compiled petrographic properties of shale caprocks from eight carbon storage sites and showed that illitic clay is the most prominent mineral (can be up to 70% of the caprock). In sandstone reservoirs, illite can constitute up to 18% of the rock mass (31).

In addition to being common in the deep subsurface sediment rocks, muscovite is widely used in material sciences research and in many engineering processes, because of its high chemical and physical stability, and as large and easily cleaved tetrahedral–octahedral–tetrahedral sheets. Upon cleaving, muscovite yields atomically smooth and large basal surfaces. Because of these properties, we chose muscovite as the model nonswelling 2:1 phyllosilicate mineral to study. Its formula $KAl_2(AlSi_3O_{10})(F,OH)_2$ represents two ditrigonal tetrahedral (T) Si sheets (with ∼25% Al substitution) and an octahedral (O) Al sheet in between. Muscovite dissolution rates increase with acidity (important for water equilibrated with CO_2) and alkalinity (32). Illite and muscovite are both dioctahedral 2:1 layered phyllosilicate minerals, and they have similar 00l reflection positions. They are

Significance

Reliable estimates of geologic carbon storage capacities (needed for policymaking) in both saline aquifers and unconventional gas/oil shales rely on understanding trapping mechanisms. We found that CO_2 uptake by muscovite (a common mineral and a conservative proxy for illite) far exceeds the maximum adsorption capacity of its external surface area. Our measurements using different methods collectively suggest that CO_2 enters muscovite interlayers without bulk interlayer expansion, contrary to the conventional wisdom that only swelling clays take up CO_2 into interlayers. Because the nonswelling illitic clay is the major clay mineral in deep subsurface tight rocks, their excess uptake of CO_2 may significantly contribute to CO_2 storage capacity and warrants further in-depth studies.

Author contributions: J.W. designed research; J.W., T.K.T., P.D.A., Y.K., M.V., and B.G. performed research; J.W., T.K.T., P.D.A. and Y.K. analyzed data; J.W., T.K.T., and D.J.D. wrote the paper; and D.J.D. was also responsible for funding.

Reviewers: A.B., Heriot-Watt University; and A.K., Institut Mines-Télécom Atlantique.

The authors declare no conflict of interest.

This open access article is distributed under Creative Commons Attribution-NonCommercial-NoDerivatives License 4.0 (CC BY-NC-ND).

[1]To whom correspondence may be addressed. Email: jwan@lbl.gov or djdepaolo@lbl.gov.

This article contains supporting information online at www.pnas.org/lookup/suppl/doi:10.1073/pnas.1710853114/-/DCSupplemental.

differentiated by diffraction of random-ordered mounts (33). Illite has a small number (<5%) of smectite interlayers. Muscovite does not have any interstratified layers with smectite. Thus, using muscovite as a proxy of illite to evaluate its reactivity with $scCO_2$ is appropriate, although probably not the other way around. It was reported that Cs^+ ions can intercalate into frayed edges of illite interlayers, resulting in interlayer expansion (34). Hu et al. (35) and Hu and Jun (36) investigated biotite dissolution in CO_2-saturated brine and observed surface cracking and formation of illite, goethite, and kaolinite. They speculated that CO_2 intercalation into biotite interlayers upon exposure to $scCO_2$ saturated brines. Although biotite is less common in deep subsurface sedimentary rocks due to its high reactivity and transformation to illite and kaolinite, it does share the common mica structure with muscovite. Molecular dynamics simulations of CO_2 diffusion within muscovite interlayers predict that transport may be significant when the slit pore dimensions are >0.25 nm (37). Gases trapped within muscovite interlayers and released during cleaving in ultrahigh vacuum amounted to 0.1–1 molecules per nanometer squared of cleaved surface area (38). Wan et al. (11) observed blisters at muscovite surface upon reaction with water–$scCO_2$, and they speculated that the blisters are possibly the result of $scCO_2$ diffusion into the interlayer from the edges of the mica plate and gas expansion upon depressurization. That conjecture motivated further research presented here. It should be noted that the atomic force microscopy (AFM) images presented in figure 7 in Wan et al. (11) contained contaminants in addition to blisters (distinguished by the phase images that we realized later).

To investigate how muscovite responds to CO_2 exposure under deep subsurface conditions, we incubated single muscovite plates (highest purity of commercially available natural crystals, freshly cleaved) first with four different fluids under otherwise identical conditions—wet-$scCO_2$, dry-$scCO_2$, wet-scN_2, and $scCO_2$-saturated brine—and then focused experiments on the most relevant and interesting fluid: water-saturated-$scCO_2$. The experiments were conducted at 12 MPa and 90 °C in a high-pressure and -temperature vessel, over times ranging from 7 d up to 1 mo. The incubation experiment setup is shown in Fig. S1. Then, a series of measurements were conducted on the reacted and unreacted control samples. The morphology of basal surfaces was examined with AFM, and the interlayer spacing was measured by X-ray diffraction (XRD) (ex situ). The surface chemistry was examined by X-ray photoelectron spectroscopy (XPS). An off-gassing experiment from reacted muscovite plates was performed to measure CO_2 release from reacted muscovite plates (the off-gassing experiment setup is shown in Fig. S2).

Results

Surface Morphology of Basal Surfaces. The AFM analyses of the control sample showed atomically smooth basal surfaces with measured roughness equal to the instrument limit (Fig. 1*E* and Fig. S3 *A*, *Middle*). For the samples incubated with $scCO_2$-saturated brine (sample was submerged into 10 mM NaCl solution that coexisted with $scCO_2$), the basal surfaces were roughened, indicative of muscovite dissolution (Fig. S3 *B*, *Middle*). For the samples incubated with dry-$scCO_2$ and wet-scN_2, the images show sparsely distributed adventitious nanoparticles that are considered practically unavoidable on high-energy muscovite surfaces (39). Surprisingly, dome-shaped features were observed on the basal surfaces of samples incubated in wet-$scCO_2$, but not under the other conditions. Fig. 1 *A*–*D* and *F*–*I* shows two selected areas from different samples. The homogeneity of the phase images (Fig. 1 *D* and *I*) indicates that the surfaces are chemically uniform (indicating no contamination). The slight variations in phase are predominately associated with changes in amplitude (Fig. 1 *C* and *H*) due to topography, but the phase shift associated with the large feature in Fig. 1 *A*–*D* indicates that it has a lower stiffness than unaltered mica. The topographic variations are not caused by deposition of foreign material or

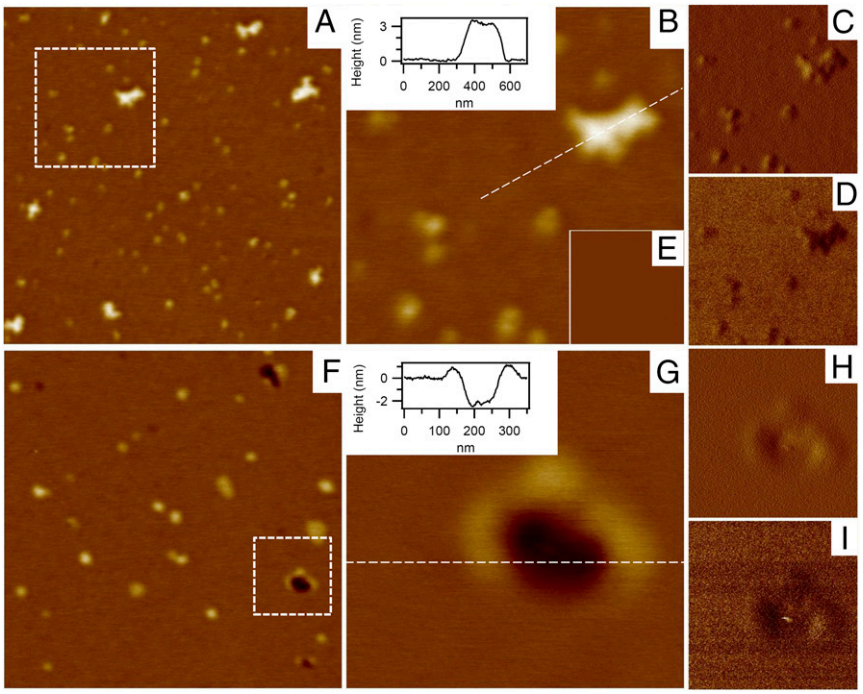

Fig. 1. AFM images of muscovite basal surface showing blistering after exposure to moist supercritical CO_2. (*A*) A 3-μm-height image. (*B*–*D*) A 1-μm zoom-in of boxed region of *A* with section across a blister (*B*) including amplitude (*C*) and phase (*D*) data. (*E*) Height image of freshly cleaved mica as baseline instrument noise. (*F*) A 2-μm-height image. (*G*–*I*) A 350-nm zoom in of boxed region of *F* with section across a collapsed blister (*G*) including amplitude (*H*) and phase (*I*) data. All height images have an 8-nm color scale. In *B* and *G*, height profiles along dashed lines are shown in *Inset* graphs.

contamination onto the basal surface. The structures are distributed over the basal surface, with sizes ranging from tens to hundreds of nanometers across and up to 2–3 nm tall. We did not observe significant variations in feature size and population with incubation time (7 and 14 d). We also did not observe discernable variations in size or population at different distances from the edges of muscovite plates. We interpreted the domed features to be blisters formed by the expansion of CO_2 intercalated into mica when the reactor vessel was depressurized from 12 MPa. Because the blistering occurred only on the samples incubated with wet-$scCO_2$, it appears that the water film is required for CO_2 entry. We also found numerous examples of features that appeared to be collapsed blisters (e.g., Fig. 1 *F–I*), suggesting escape of trapped CO_2 from local surface defects after depressurization. It is worth noting that we do not expect blisters to form under subsurface conditions because depressurization and gas expansion do not occur.

Interlayer d-Spacing Measurements. The ex situ XRD measurements obtained on single muscovite plates (samples previously incubated under elevated pressure and temperature, then measured under 1-atmosphere pressure conditions) showed no alteration of the basal spacing; with measured values of $d(002)$ spacing 9.97 ± 0.028 Å in both control and wet-$scCO_2$–incubated plates, consistent with the standard value (40). The bulk muscovite interlayers did not swell in response to exposure to $scCO_2$. Indeed, d-spacing alteration of bulk samples is not expected, giving the strong electrostatic binding between interlayer K^+ and the negative charges localized in the immediately adjacent silicate layers (41).

Chemical Characterization of the Basal Surface. XPS is a surface-sensitive spectroscopic technique. Approximately 95% of the detected photoelectrons originate from the surface down to the depth of 3λ, with λ being the electron inelastic mean free path. In muscovite, λ ∼ 0.86–0.88 nm for photoelectrons associated with the C 1s binding energy (283–290 eV) (42); thus, 3λ can include C photoelectrons emanating from the upper surface down through the two interlayers. The XPS analyses were conducted to compare freshly cleaved muscovite samples with samples exposed to $scCO_2$-saturated brine, and to water-saturated $scCO_2$. Survey scans showed peaks for expected muscovite elements: Al, Si, O, K, and, in a few cases, F. In addition, the only non-muscovite element present was C. Analysis of the control sample yielded 150 ppm total C (total organic carbon/total inorganic carbon analyzer; Shimadzu TOC-VCPH), even though it was considered of highest purity. High-resolution XPS scans were conducted over the O 1s region to calibrate spectra to the O 1s peak at 531.4 eV for muscovite (43) and over the C 1s and K 2p energy regions (Fig. 2). Suitability of the calibrations to the O 1s peaks was demonstrated through good agreement of the K 2p peaks with literature values (43). All samples including the control displayed C 1s peaks of varying intensity in the organic/adventitious/graphitic region at ∼285–284 eV, and most also contained a peak in the range of 282–281 eV associated with carbidic C (43). Native and adventitious C of reduced-organic nature have previously been reported in XPS measurements of freshly air-cleaved muscovite (39, 44), and the highest-grade muscovite has been reported to contain graphitic carbon.

Unique to samples incubated in wet $scCO_2$ was a distinct peak at ∼290.5 eV, adjacent to the K 2p3/2 peak. No evidence of resonance in the vicinity of 290.5 eV was observed for either the control sample or the muscovite incubated in CO_2-saturated brine. It should be noted that the carbidic, graphitic, and organic C peaks all occurred at binding energies that were significantly lower than those associated with CO_2 and carbonates. Note that physisorbed CO_2 would only be expected to persist with (at most) monolayer coverage on basal surfaces after samples were returned to atmospheric pressure and that most of this CO_2 should be desorbed during evacuation of the XPS sample chamber (10^{-9} torr) before collection of XPS data. Thus, it is reasonable to believe that the measured peak at ∼290.5 eV is interlayer trapped CO_2. Previously, Bhattacharyya (44) detected very small amounts of C adsorption on muscovite (C 1s peak intensity ∼15% that of K 2p3/2) following low pressure (10^{-5} torr) exposure to CO_2, and loss of CO_2 with exposure to higher vacuum (44). Time-dependent losses of CO_2 from our $scCO_2$-exposed muscovite were evident from the decreases in the 290.5-eV peak (Fig. 2) through collection of spectra at the same spot for three to four times within up to 4 h under the ultrahigh vacuum. This suggested that CO_2 diffused out of the near-surface interlayers during the course of the measurement in the vacuum chamber. We therefore designed a separate off-gassing experiment that allowed quantification of CO_2 release from muscovite.

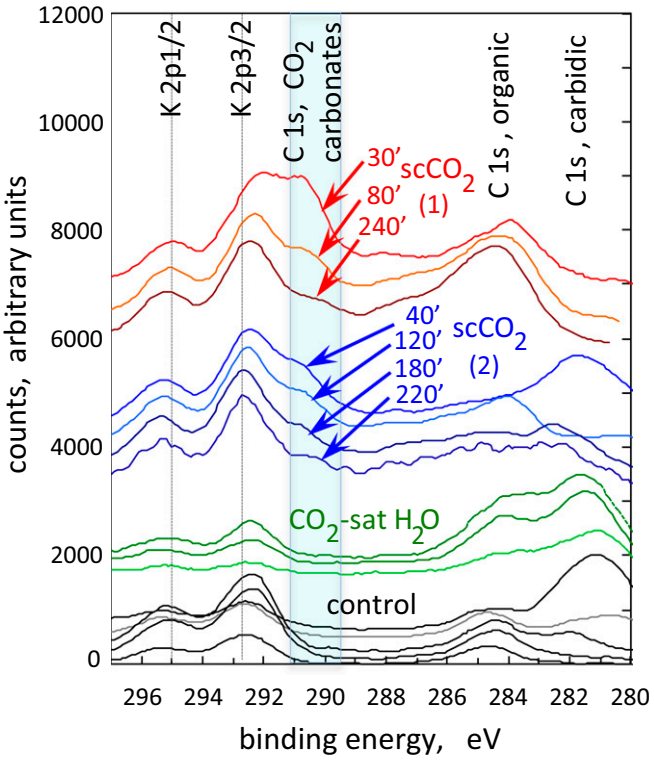

Fig. 2. XPS high-resolution scans indicating interlayer CO_2 and CO_2 releasing as time in vacuum. The distinct C 1s peak at 290.5 eV (CO_2) appeared only on samples incubated with wet-$scCO_2$ and was absent from the control and CO_2-saturated brine-incubated samples. Note the intensity of C 1s peak collected at a single location decreased with time (30–240 min for one sample and 40–220 min for another) under the 10^{-9} Torr vacuum. Spectra for the other conditions were collected at randomly selected locations on samples, generally within 0.5–3 h after removal from the reactor.

Off-Gassing of CO_2 from Reacted Muscovite Samples. To quantify adsorbed and surface region-associated CO_2, off-gassing measurements were performed through comparing samples exposed to wet-$scCO_2$ with control samples. Each sample consisted of six small muscovite plates with the total surface areas of 33.6 cm^2 from basal surfaces and 1.5 cm^2 from edges. For the $scCO_2$-exposed samples, the mica plates were transferred to a N_2 glove bag after removal from the depressurized reactor, to purge weakly sorbed CO_2 off external surfaces of samples, then sealed in a glass serum bottle for later analyses of off-gassed CO_2 (photographs of the sample vials are shown in Fig. S2). The results presented in Fig. 3*A* show the cumulative CO_2 released

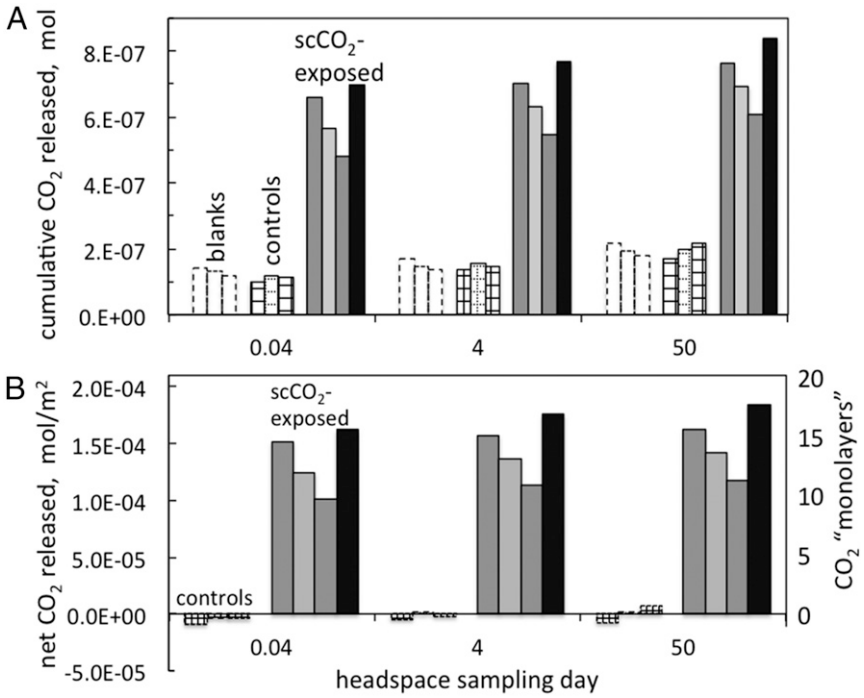

Fig. 3. Comparison of CO_2 release with bulk surface area, indicating CO_2 interlayer uptake. (*A*) Cumulative CO_2 recovered from blank (sealed empty vials), control, and $scCO_2$-exposed samples of three or four replicates. (*B*) Blank-subtracted CO_2 recovery per unit bulk surface area of muscovite (left vertical axis) and as equivalent numbers of CO_2 monolayers (right vertical axis).

from each of three or four replicate samples. The CO_2 recovered from the control samples showed amounts similar to those obtained from the blanks (empty serum bottles), reflecting a low background CO_2 off-gassed from the septum stoppers.

In contrast, $scCO_2$-exposed muscovite samples yielded approximately seven times more CO_2 relative to the controls and blanks. After subtracting the average of blank samples, the controls were found to release negligible CO_2. Fig. 3*B* shows CO_2 release per unit bulk surface area of the muscovite plates along the left vertical axis. Using an area of 0.16 nm^2 per CO_2 molecule (45), the cumulative CO_2 released was also expressed in terms of equivalent monolayer thicknesses along the right vertical axis of Fig. 3*B*. A condensed film of ∼15 molecular layers of CO_2 on the exterior surfaces of muscovite clearly was not present after depressurization of the reactor and removal of the samples within the purged N_2 glove bag. While large, this amount of released CO_2 was insignificant compared with the storage capacity expected if intercalation was pervasive, because each ∼0.3-mm-thick muscovite plate contained $\sim 3 \times 10^5$ interlayers. We therefore conclude that the CO_2 recovered in the off-gassing experiment must have originated from shallow depths in exposed, $scCO_2$-reacted basal surfaces and along edges disturbed during cutting of plates.

Discussion and Implications

Although the AFM, XPS, and off-gassing measurements of control vs. wet-$scCO_2$–reacted samples suggested possible CO_2 intercalation into muscovite interlayers, the XRD measurements showed no interlayer expansion. A key question is whether CO_2 molecules can diffuse into muscovite interlayers without expansion. The interlayer widths between centers of two opposite oxygen planes was ∼0.34 nm (44, 46), which, upon accounting for oxygen radii (0.121 nm) (47), left a minimum gap of only 0.10 nm (Fig. 4*A*). The separations between O on individual Si tetrahedral provided wider channels, ∼0.2 nm, within interlayers. However, these channels were substantially smaller than the 0.33-nm kinetic diameter for CO_2 (48). Even the smaller diameters proposed for the effective cross-section of CO_2, ranging from 0.31 (45) to 0.232 nm (49), remained prohibitively large, and K^+ occupying all siloxane cavities present in-plane obstacles (Fig. 4*B*). While previous studies showed release of CO_2 (48) and even larger molecules N_2 (0.364–0.380 nm) and CO (0.369 nm) (38) from muscovite interlayers, and our AFM, XPS, and off-gassing analyses collectively showed the CO_2 interlayer trapping, our comparisons of interlayer dimensions and molecular sizes suggest that these gases cannot intercalate the interlayers of an undisrupted crystal structure.

Based on these interlayer dimensions and molecular size considerations and the lack of increased blistering near the edges of the muscovite plates, as well as the muscovite solubility considerations in the $scCO_2$-acidified water films described below, we hypothesize that CO_2 enters mainly through local defects formed on basal surfaces rather than by diffusing from the edges deeply into interlayers. Our experiment results showed that only the reaction with wet-$scCO_2$ caused blistering, while scN_2, dry-$scCO_2$, and $scCO_2$-saturated brine did not. This suggests that a $scCO_2$-acidified water film between bulk $scCO_2$ and muscovite is the necessary condition for CO_2 molecules to enter the interlayers. Previous studies have predicted and demonstrated the stability of nanometer-scale brine films on muscovite under $scCO_2$ confinement (50, 51). Knauss and Wolery (52) reported that muscovite dissolution rates increased as pH decreased <0.1 MPa and 70 °C. Assuming a pH of 2.9 for the brine film (53) and a dissolution rate of 1.7×10^{-12} mol·m^{-2}·s^{-1} (52) leads to a predicted average dissolution depth of 0.15 nm within 7 d of reaction. Nonuniform distributions of Al substitutions for Si may lead to localized sites on basal surfaces that are more susceptible to dissolution in the adsorbed $scCO_2$-acidified water films, allowing CO_2 to enter damaged locations under elevated pressure and temperature. Vacancies of K^+ ions and the other crystal defects could provide the necessary spaces for CO_2 entry. The volume fraction associated with these defects would be too small to affect XRD measurements of bulk samples. Although this hypothesis on the mechanism for CO_2 intercalation needs further

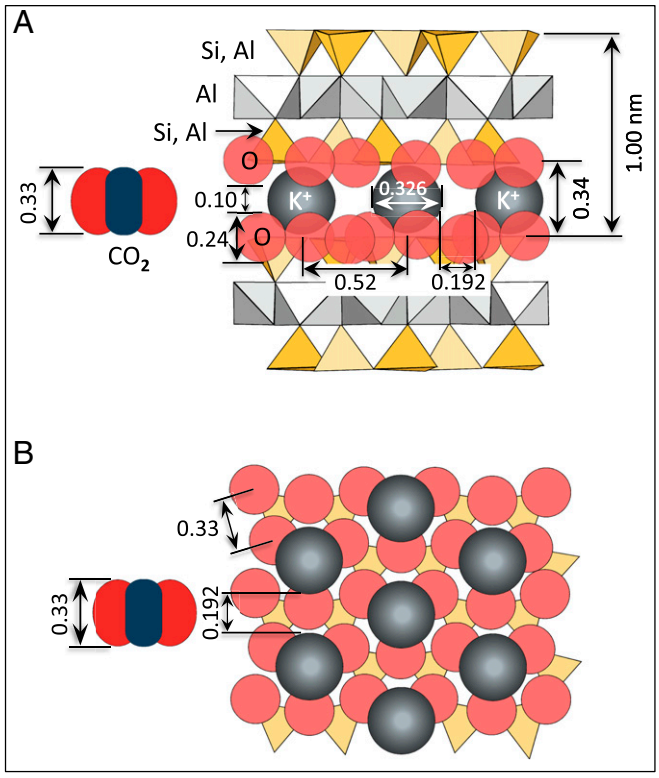

Fig. 4. Comparisons between muscovite interlayer dimensions and assumed 0.33-nm kinetic diameter of CO_2. (*A*) Edge view, showing 0.34-nm average distance between centers of two oxygen on opposing ditrigonal silica sheets result in minimum gaps of ∼0.10 nm. (*B*) Basal surface view, showing the occupancy of all ditrigonal cavities by K^+ imposes additional 0.19-nm constrictions within the interlayer plane.

testing, our calculated additional CO_2 storage capacity in reservoirs based on the measured CO_2 uptake by muscovite shows the significance of this partitioning.

The potential significance of CO_2 uptake by muscovite, and by extension onto illite, on enhancing reservoir storage capacity becomes evident upon comparison with storage attributable to capillary trapping, one of the main CO_2 storage mechanisms (1, 2). The muscovite/illite-associated CO_2 capacity can be approximated as the product of equivalent CO_2 uptake per muscovite/illite surface area times the abundance of this surface area per bulk volume of reservoir rock. As shown in *Supporting Information* (Tables S1 and S2), CO_2 partitioning onto muscovite/illite under representative reservoir conditions may amount to as much as 30% of the capacity expected from capillary trapping in sandstone (Fig. S4). Future measurements of CO_2 excess sorption isotherms on muscovite could provide additional insights into partitioning over a broad range of reservoir pressures.

The results presented in this work are the beginning stages toward understanding CO_2 uptake by nonswelling clays. The pathways for CO_2 entering the interlayers are still hypotheses needing more testing, especially under in situ (high-pressure and -temperature) conditions. The rates and extent of the CO_2 uptake, and dependence on varying geochemical conditions, need to be quantified to apply this knowledge. We hope this preliminary research will stimulate more creative studies on this topic, especially given the abundance of illite and muscovite, and their importance in many energy and environment issues.

Materials and Methods

Materials. V-1–grade natural muscovite plates (catalog no. 71855-05; Electron Microscopy Sciences) were used. High-purity CO_2 (99.99%; Praxair), ultrapure deionized water (resistivity ≥18 MΩ; Milli-Q), and American Chemical Society-grade chemicals were used. Muscovite plates (70 × 25 × 0.3 mm thick) were cut and then cleaved to ∼35 × 8 × 0.2 mm before placement in the reactor. The cleaved fresh surfaces were marked, and only the fresh surfaces were used for after-reaction AFM and XPS characterizations.

High P-T Muscovite–CO_2 Incubation. The incubations were conducted in a high-pressure–temperature Hastelloy vessel (Parr; model 4560), with the pressure controlled by an ISCO pump (model 500HP; Teledyne ISCO) and temperature-controlled by a Parr Temperature Control Module. The pressure (12 ± 0.01 MPa) and temperature (90 ± 0.1 °C) were constants through the experiments. Under these pressure and temperature conditions, water solubility in $scCO_2$ was ∼1.5%, and CO_2 in water was ∼1.8% (54). The reaction durations were 7, 14, and 30 d for different tests. Each experiment was repeated three times or more, with much attention given to avoiding potential mica surface contamination. For the reaction with CO_2-saturated brine, both the inside and outside of the polytetrafluoroethylene (PTFE) bottle were filled with brine up to the holes of the PTFE bottle, and the remaining space was filled with $scCO_2$. For the reaction with water-saturated-$scCO_2$, 3 mL of deionized water was placed inside the bottom of the vessel, outside the PTFE container, to ensure water saturation in $scCO_2$ without direct contact between muscovite plate and bulk water. For the reaction with dry-$scCO_2$, no water added in the reactor and the pure CO_2 was used as-is from the tank. The experiment setup is illustrated in Fig. S1.

AFM. The nanometer-scale surface morphological features of the control and reacted samples were quantified by using the tapping mode on a Bruker Icon AFM. Height, amplitude, and phase images were collected simultaneously. Tap150-G (BudgetSensors) tips were used (drive frequencies were ∼150 kHz, and scan rates ranged between 0.3 and 1 Hz). For each sample, at least five areas over the basal surface were analyzed, and at each area, several images at different scales were recorded. The Nanoscope Analysis software (Version 1.40; Bruker) was used to analyze the images and calculate the area and line roughness.

XPS. XPS (Physical Electronics PHI 5300) was used to determine the chemical composition of the basal surface for unreacted muscovite and samples reacted with CO_2-saturated brine and water-saturated $scCO_2$. The spectra were acquired with an Al K_α X-ray source operated at 1,486.6 eV and 350 W (15 kV–25 mA) in a 10^{-9} torr vacuum chamber. Measurements were taken with sample stage flat (take-off angle of 35.3° from the surface). Survey spectra were acquired with 1 eV per step and pass energy of 178.95 eV. High-resolution scans were acquired with 0.1 eV per step and 35.75 eV pass energy. The energy axis was calibrated by setting the O 1s peak to 531.4 eV on the high-resolution scan (43, 55). After calibration, the Al 2p, Si 2p3/2, and K 2p3/2 peaks all lined up within 0.4 eV of their reference values (74.1, 102.4, and 292.8 eV, respectively) for muscovite (43).

XRD. For the ex situ XRD measurements, muscovite monocrystals (∼45 × 12.5 × 0.2 mm) were used for both control and reacted samples, with the latter incubated in water-saturated $scCO_2$ for 14 d. The diffraction pattern was collected ∼2 h after the beginning of depressurizing the high-P reactor. XRD spectra were collected on a powder diffractometer PANalytica X'Pert pro (Co K_α radiation, 40 kV, 40 mA, X'Celerator detector). Since the samples were single crystals, they were mounted on spinner sample holder, with the basal plane as the sample surface. This procedure simulated a perfectly oriented polycrystal, allowing collecting of all the valid (00*l*) reflections of muscovite (and only those) in a powder-like diffraction profile, allowing a precise measurement of the basal *d*-spacing.

Off-Gassing of CO_2 from Muscovite. This experiment was designed to help determine whether or not CO_2 entered muscovite interlayers by comparing samples exposed to wet-$scCO_2$ with unexposed control samples. Each sample (four replicates for CO_2-incubated and triplicate for controls) consisted of six small plates (35 × 8 × 0.3 mm). Each sample had an external surface area of 35 cm^2, primarily from basal surfaces (33.6 cm^2), with a smaller contribution from edges (1.5 cm^2). The high P-T muscovite–CO_2 incubation and sampling steps were conducted as described above (instead of one plate at a time, the 24 small plates were all in one PTFE bottle). After opening the Parr reactor, the PTFE bottle containing all of the mica plates was brought into a N_2 glove bag and transferred to a glass dish. The N_2 bag was then vacuumed and refilled two times to remove the surface-accumulated CO_2 and free CO_2. Then, six small plates were placed into a 25.6-mL glass serum bottle under the N_2 atmosphere and sealed with a thick blue chlorobutyl septum stopper (Fig. S2). Sampling of

the headspace in each bottle, including triplicate empty (blank) bottles, was done by initially collecting 60 mL of gas into a syringe ~1 h after sealing. Two subsequent 20-mL gas samples were collected from each bottle at 4 and 15 d. The sampled gas was immediately injected into the N_2 carrier gas stream flowing into a CO_2 gas analyzer (Li-Cor LI-840A) (56). The cumulative CO_2 recovered from the $scCO_2$-exposed and control samples were compared after subtraction of measurements obtained on blank samples.

ACKNOWLEDGMENTS. We thank Virginia Altoe for instructions and assistance with XPS measurements and Andrey Kalinichev and Andreas Busch for the helpful discussions and review of this manuscript. This work was supported by the Center for Nanoscale Control of Geologic CO_2, an Energy Frontier Research Center funded by the Department of Energy, Office of Science, and Office of Basic Energy Sciences under Award DE-AC02-05CH11231. Work at the Molecular Foundry was supported by the Office of Science, Office of Basic Energy Sciences, of the Department of Energy under Contract DE-AC02-05CH11231.

1. Benson SM, Cole DR (2008) CO_2 sequestration in deep sedimentary formations. *Elements* 4:325–331.
2. Bachu S, et al. (2007) CO_2 storage capacity estimation: Methods and gaps. *Int J Greenhouse Gas Control* 1:430–443.
3. Barati R, Liang JT (2014) A review of fracturing fluid systems used for hydraulic fracturing of oil and gas wells. *J Appl Polym Sci* 131:40735.
4. Middleton RS, et al. (2015) Shale gas and non-aqueous fracturing fluids: Opportunities and challenges for supercritical CO_2. *Appl Energy* 147:500–509.
5. Kowalczyk P, Furmaniak S, Gauden PA, Terzyk AP (2010) Carbon dioxide adsorption-induced deformation of microporous carbons. *J Phys Chem C* 114:5126–5133.
6. Busch A, et al. (2016) On sorption and swelling of CO_2 in clays. *Geomech Geophys Geo-Energy Geo-resour* 2:111–130.
7. Gaus I (2010) Role and impact of CO_2–rock interactions during CO_2 storage in sedimentary rocks. *Int J Greenhouse Gas Control* 4:73–89.
8. Chiquet P, Broseta D, Thibeau S (2007) Wettability alteration of caprock minerals by carbon dioxide. *Geofluids* 7:112–122.
9. Kim Y, Wan J, Kneafsey TJ, Tokunaga TK (2012) Dewetting of silica surfaces upon reactions with supercritical CO_2 and brine: Pore-scale studies in micromodels. *Environ Sci Technol* 46:4228–4235.
10. Jung J-W, Wan J (2012) Supercritical CO_2 and ionic strength effects on wettability of silica surfaces: Equilibrium contact angle measurements. *Energy Fuels* 26:6053–6059.
11. Wan J, Kim Y, Tokunaga TK (2014) Contact angle measurement ambiguity in supercritical CO_2-water-mineral systems: Mica as an example. *Int J Greenhouse Gas Control* 31:128–137.
12. Tokunaga TK, Wan J (2013) Capillary pressure and mineral wettability influences on reservoir CO_2 capacity. *Rev Mineral Geochem* 77:481–503.
13. Tokunaga TK, et al. (2013) Capillary pressure and saturation relations for supercritical CO_2 and brine in sand: High-pressure $P_c(S_w)$ controller/meter measurements, and capillary scaling predictions. *Water Resour Res* 49:4566–4579.
14. Wang S, Tokunaga TK (2015) Capillary pressure-saturation relations for supercritical CO_2 and brine in limestone/dolomite sands: Implications for geologic carbon sequestration in carbonate reservoirs. *Environ Sci Technol* 49:7208–7217.
15. Hu R, Wan J, Kim Y, Tokunaga TK (2017) Wettability effects on supercritical CO_2-brine immiscible displacement during drainage: Pore-scale observation and 3D simulation. *Int J Greenhouse Gas Control* 60:129–139.
16. Hu R, Wan J, Kim Y, Tokunaga TK (2017) Wettability impact on supercritical CO_2 capillary trapping: Pore-scale visualization and quantification. *Water Resour Res* 53: 6377–6394.
17. Busch A, et al. (2008) Carbon dioxide storage potential of shales. *Int J Greenhouse Gas Control* 2:297–308.
18. Heller R, Zoback M (2014) Adsorption of methane and carbon dioxide on gas shale and pure mineral samples. *J Unconv Oil Gas Resour* 8:14–24.
19. Wilson MJ, Shaldybin MV, Wilson L (2016) Clay mineralogy and unconventional hydrocarbon shale reservoirs in the USA. I. Occurrence and interpretation of mixed-layer R3 ordered illite/smectite. *Earth Sci Rev* 158:31–50.
20. Gaudette HE, Eades JL, Grim RE (1963) The nature of illite. *Clays Clay Miner* 41:33–48.
21. Loring JS, et al. (2012) In situ molecular spectroscopic evidence for CO_2 intercalation into montmorillonite in supercritical carbon dioxide. *Langmuir* 28:7125–7128.
22. Ilton ES, Schaef HT, Qafoku O, Rosso KM, Felmy AR (2012) In situ X-ray diffraction study of Na+ saturated montmorillonite exposed to variably wet super critical CO_2. *Environ Sci Technol* 46:4241–4248.
23. Schaef HT, et al. (2012) In situ XRD study of Ca2+ saturated montmorillonite (STX-1) exposed to anhydrous and wet supercritical carbon dioxide. *Int J Greenhouse Gas Control* 6:220–229.
24. Romanov VN (2013) Evidence of irreversible CO_2 intercalation in montmorillonite. *Int J Greenhouse Gas Control* 14:220–226.
25. Rother G, et al. (2012) Pore size effects on the sorption of supercritical CO_2 in mesoporous CPG-10 silica. *J Phys Chem C* 116:917–922.
26. Rao Q, Leng Y (2016) Molecular understanding of CO_2 and H2O in a montmorillonite clay interlayer under CO_2 geological sequestration conditions. *J Phys Chem* 120: 2642–2654.
27. Rother G, et al. (2013) CO_2 sorption to subsingle hydration layer montmorillonite clay studied by excess sorption and neutron diffraction measurements. *Environ Sci Technol* 47:205–211.
28. Giesting P, Guggenheim S, Koster van Groos AF, Busch A (2012) X-ray diffraction study of K- and Ca-exchanged montmorillonites in CO_2 atmospheres. *Environ Sci Technol* 46:5623–5630.
29. Giesting P, Guggenheim S, van Groos AFK, Busch A (2012) Interaction of carbon dioxide with Na-exchanged montmorillonite at pressures to 640 bars: Implications for CO_2 sequestration. *Int J Greenhouse Gas Control* 8:73–81.
30. Espinoza DN, Santamarina JC (2012) Clay interaction with liquid and supercritical CO_2: The relevance of electrical and capillary forces. *Int J Greenhouse Gas Control* 10: 351–362.
31. Norden B, et al. (2010) Lithological and petrophysical core-log interpretation in CO2SINK, the European CO_2 onshore research storage and verification project. *SPE Reservoir Eval Eng* 13:179–192.
32. Kalinowski BE, Schweda P (1996) Kinetics of muscovite, phlogopite, and biotite dissolution and alteration at pH 1-4, room temperature. *Geochim Cosmochim Acta* 60: 367–385.
33. Altaner SP, Ylagan RF (1997) Comparison of structural models of mixed-layer illite/smectite and reaction mechanisms of smectite illitization. *Clays Clay Miner* 45: 517–533.
34. Fuller AJ, et al. (2015) Caesium incorporation and retention in illite interlayers. *Appl Clay Sci* 108:128–134.
35. Hu Y, Ray JR, Jun YS (2011) Biotite-brine interactions under acidic hydrothermal conditions: Fibrous illite, goethite, and kaolinite formation and biotite surface cracking. *Environ Sci Technol* 45:6175–6180.
36. Hu Y, Jun YS (2012) Biotite dissolution in brine at varied temperatures and CO_2 pressures: Its activation energy and potential CO_2 intercalation. *Langmuir* 28: 14633–14641.
37. Cole DR, Chialvo AA, Rother G, Vlcek L, Cummings PT (2010) Supercritical fluid behavior at nanoscale interfaces: Implications for CO_2 sequestration in geologic formations. *Philos Mag* 90:2339–2363.
38. Mercer PD (1967) Analysis of the gases released on cleaving muscovite mica in ultrahigh vacuum and of gases which remain adsorbed on the freshly cleaved surface. *Vaccume* 17:267–270.
39. Israelachvili JN, Alcantar NA, Maeda N, Mates TE, Ruths M (2004) Preparing contamination-free mica substrates for surface characterization, force measurements, and imaging. *Langmuir* 20:3616–3622.
40. Guidotti CV (1984) *Micas in Metamorphic Rocks* (Mineralogical Society of America, Chantilly, VA), 1st Ed.
41. Deer WA, Howie RA, Zussman J (2013) *An Introduction to the Rock-Forming Minerals* (Mineralogical Society of Great Britain and Ireland, London), 3rd Ed, p 498.
42. Tanuma S, Powell CJ, Penn DR (1991) Calculations of electron inelastic mean free paths. II. Data for 27 elements over the 50 – 2000 eV range. *Surf Interface Anal* 17: 911–926.
43. National Institute of Standards and Technology (2012) Matches from Compound Name Search of muscovite. Available at srdata.nist.gov/xps/query_chem_name_detail.aspx?ID_NO=1785&CName=micamuscovite. Accessed May 31, 2017.
44. Bhattacharyya KG (1989) Adsorption of carbon-dioxide on mica surfaces. *Langmuir* 5: 1155–1162.
45. Koresh J, Soffer A (1980) Study of molecular-sieve carbons. 2. Estimation of cross-sectional diameters of non-spherical molecules. *J Chem Soc Faraday Trans I* 76: 2472–2485.
46. Guggenheim S, Chang YH, Vangroos AFK (1987) Muscovite dehydroxylation—high-temperature studies. *Am Mineral* 72:537–550.
47. Shannon RD (1976) Revised effective ionic-radii and systematic studies of interatomic distances in halides and chalcogenides. *Acta Crystallogr A* 32:751–767.
48. Li JR, Kuppler RJ, Zhou HC (2009) Selective gas adsorption and separation in metal-organic frameworks. *Chem Soc Rev* 38:1477–1504.
49. Lucia A, Bonk BM (2012) Molecular geometry effects and the Gibbs-Helmholtz constrained equation of state. *Comput Chem Eng* 37:1–14.
50. Tokunaga TK (2012) DLVO-based estimates of adsorbed water film thicknesses in geologic CO_2 reservoirs. *Langmuir* 28:8001–8009.
51. Kim TW, Tokunaga TK, Bargar JR, Latimer MJ, Webb SM (2013) Brine film thicknesses on mica surfaces under geologic CO_2 sequestration conditions and controlled capillary pressures. *Water Resour Res* 49:5071–5076.
52. Knauss KG, Wolery TJ (1989) Muscovite dissolution kinetics as a function of pH and time at 70 °C. *Geochim Cosmochim Acta* 53:1493–1501.
53. Toews KL, Shroll RM, Wai CM, Smart NG (1995) Ph-defining equilibrium between water and supercritical CO_2—influence on SFE of organics and metal-chelates. *Anal Chem* 67:4040–4043.
54. Spycher N, Pruess K, Ennis-King J (2003) CO_2-H_2O mixtures in the geological sequestration of CO_2. I. Assessment and calculation of mutual solubilities from 12 to 100 degrees C and up to 600 bar. *Geochim Cosmochim Acta* 67:3015–3031.
55. Wagner CD, et al. (1982) Auger and photoelectron line energy relationships in aluminum–oxygen and silicon–oxygen compounds. *J Vac Sci Technol* 21:933–944.
56. Davidson EA, Trumbore SE (1995) Gas diffusivity and production of CO_2 in deep soils of the Eastern Amazon. *Tellus B Chem Phys Meterol* 47:550–565.